Proceedings of the Seventh International Conference on
Railway Technology: Research, Development and Maintenance
Edited by: J. Pombo
Civil-Comp Conferences, Volume 15, Paper 5.4
Civil-Comp Press, Edinburgh, United Kingdom, 2026
ISSN: 2753-3239, doi: 10.4203/ccc.15.5.4

Effect of the Ground Modeling Method on Aerodynamic Noise Characteristics of High-speed Trains

W. Lu

**Institute of Mechanics, Chinese Academy of Sciences,
Beijing, China**

Abstract

To investigate the impact of different ground modeling approaches on the aerodynamic noise characteristics of high-speed trains, this study adopts a numerical simulation method based on Delayed Detached Eddy Simulation and Ffowcs Williams-Hawkings equations. Aerodynamic noise sources and sound field characteristics of a simplified three-car high-speed train are compared between flat-ground modeling and refined bridge modeling. The results show that bridge modeling narrows the flow space beneath the train, leading to fragmentation and lateral overflow of vortex structures, thereby modifying the noise spectrum distribution. Under flat-ground modeling, sound energy is concentrated in the mid-frequency range (250-1600 Hz) with higher source intensity, while bridge modeling disperses sound energy toward both low and high frequencies, resulting in an overall reduction in noise level. The study further reveals that the underbody region serves as the main noise contributor. Although bridge modeling reduces overall noise by decreasing the underbody-to-rail gap, the fragmented vortex structures simultaneously enhance low- and high-frequency noise components. In terms of far-field noise, bridge modeling yields lower sound pressure levels; however, the difference between bridge and flat-ground modeling gradually widens downstream, reaching a maximum of approximately 4 dB. This variation is attributed to the combined effects of mid-frequency sound energy peaks and high-frequency sound energy contributions.

Keywords: high-speed trains, ground modeling, aerodynamic noise, noise source, acoustic field, frequency band.

1 Introduction

The level of development of high-speed trains is an important indicator of a country's industrial capabilities [1-2]. Noise levels are one of the most important criteria for the future development of high-speed trains [3-4]. With the continuous increase in operational speeds of high-speed trains, aerodynamic noise has become the dominant acoustic source, surpassing rolling and propulsion noise at speeds typically above 300 km/h [5-6]. This aerodynamic-generated sound not only contributes to environmental noise pollution along railway lines but also affects passenger comfort and imposes strict design constraints on new train generations. Therefore, accurately predicting and effectively mitigating aerodynamic noise is paramount for the sustainable development of high-speed rail.

Extensive research has been conducted to understand and model the aerodynamic noise sources of high-speed trains [7-8]. Early numerical and experimental studies often simplified the geometry and surrounding conditions to isolate key noise sources. A common simplification involves modeling the train running on a flat, rigid ground plane [9]. This approach has successfully identified and characterized major aerodynamic noise contributors of the train, including: bogie cavities, pantographs, inter-car gaps, and etc [10-12]. Among these, the complex bogie structure renders the aerodynamic noise in the bogie area exceptionally intricate, making it the primary source of aerodynamic noise in high-speed trains [13]. The noise generation mechanism in the bogie area is primarily due to the interaction of the flow structure generated by the high-speed aerodynamic flow through the bogie cabin and the flow structure generated by the wheels, axles, and other blunt bodies in a narrow space, which is part of the coupled noise of cavities and blunt bodies in the near-ground space [14-15]. The flow around the bogie exhibits unsteady characteristics, particularly in the rear edge region of the bogie cavity where vortex structures violently impact the ground, resulting in highly turbulent flow conditions in this area [16]. It is evident that this simplified boundary condition provides valuable insights into the noise generated by underbody flow, particularly the bogie region [17].

However, the flat-ground model inherently assumes an acoustically semi-infinite space and does not account for the complex geometric configurations encountered in real-world operations. A significant portion of high-speed railway lines is composed of viaducts or bridges, especially in regions with challenging terrains[18]. The presence of a bridge structure fundamentally alters the aerodynamic and aeroacoustic environment beneath the train. Instead of a confined ground clearance, the train underbody and the bridge surface form a moving cavity, while bridge components like parapets, guardrails, and the deck itself introduce additional flow separations and sharp edges that act as potent dipole noise sources [19]. Additionally, the sleeper arrangement on the bridge results in pressure peaks near the bogies, lower minimum static pressure values, altered flow patterns in the underbody of the train, and high-frequency fluctuations [20]. The acoustic field is also significantly modified by the reflection and reverberation within the bridge structure, leading to a directivity pattern and sound pressure level distribution that differ markedly from the flat-ground scenario [21]. Consequently, relying solely on flat-ground models for noise prediction on bridge sections can lead to substantial inaccuracies in both the overall sound level and the spectral composition.

Therefore, to achieve a comprehensive and realistic assessment of aerodynamic noise from high-speed trains, it is essential to move beyond simplified flat-ground models and incorporate detailed bridge geometries. This study aims to elucidate the critical impact of bridge modeling on the accuracy of aeroacoustic simulations for high-speed trains, particularly those originating from the underbody. Using methods based on the DDES and FW-H equations, numerical simulations of the flow and noise characteristics of high-speed trains were conducted. The aerodynamic acoustic results from the flat-ground model were compared with those from the detailed bridge model. This study emphasizes the necessity of incorporating real infrastructure into noise prediction models to develop more effective and precise noise reduction strategies for bridge sections, which constitute a vital part of modern high-speed railway networks.

2 Methods

2.1 Model Description

In this paper, a simplified three-car higher-speed train model is selected as the research model, with enclosed windshields used to connect the head car to the middle car, and the middle car to the tail car. The higher-speed train model has the following dimensions: the height (*H*) is 3.7 m, the length (*L*) is 83.6 m, and the width (*W*) is 3.36 m, as illustrated in Figure. **1**. Three surface pressure fluctuation monitoring points, labeled *S1 – S3* are designated on the train model, as shown in Figure. **1** (a). These points are specifically placed at the following locations:

- *S1*: at the nose cone of the head car,
- *S2*: at the middle of the middle car,
- *S3*: at the nose cone of the tail car.

The height of points *S1 – S3* is 1.2 m, corresponding to the height of the nose cone.

The three-car train is equipped with six bogies underneath, as illustrated in **Figure. 1** (b). Among them, the bogies of the head car and the tail car are both trailer bogies, which are fitted with fairings/ web plates for noise reduction. The two bogies of the middle car are motor bogies and are not equipped with fairings/web plates.

Figure. **1** (c) and (d) show schematic diagrams of the geometric models from the front view for flat-ground modeling and bridge modeling, respectively. In both models, the train wheels are set at a height of 500 mm above the ground plane. In the bridge model, a double-track configuration is adopted, with the crash wall located at a height of 560 mm above the ground plane.

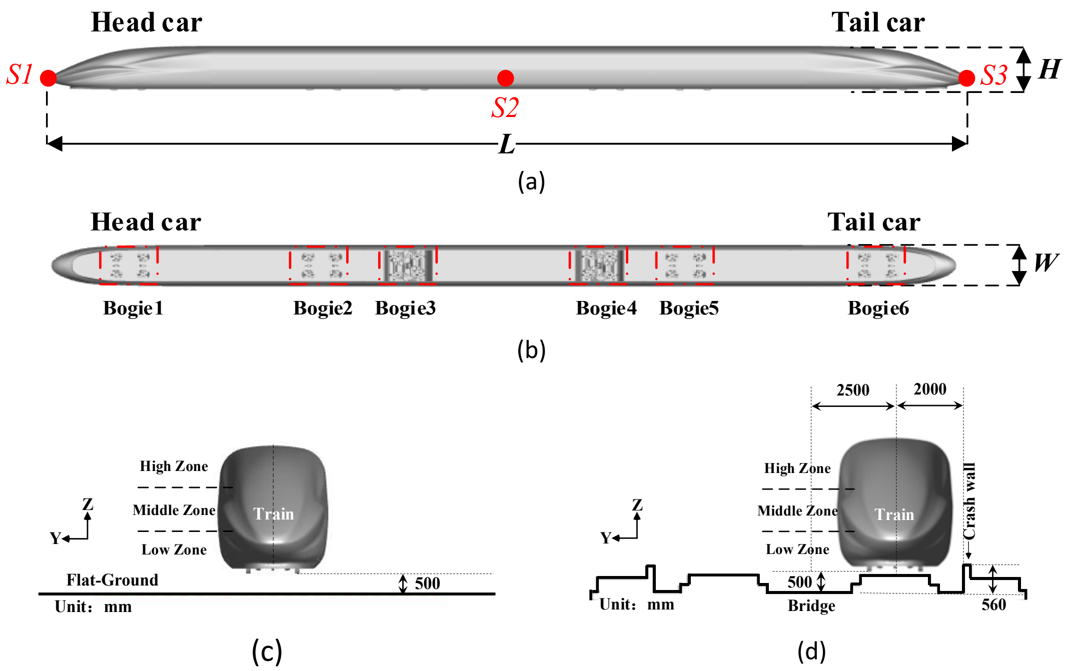

Figure. 1 Schematic diagram of high-speed train model ((a) Lateral view and surface pressure monitoring point locations; (b) Bottom view; (c) Flat-ground modelling frontal view; (d) Bridge modelling frontal view).

To further analyze the contribution of noise intensity in each region along the height direction of the high-speed train, the train's height is divided into three distinct zones, namely, High zone, Middle zone, and Low zone, as illustrated in Figure. **1** (c) and (d).

2.2. Numerical Simulation Method

In this paper, a combination of Delayed Detached Eddy Simulation (DDES) and the Ffowcs Williams-Hawkings (FW-H) equations is employed. The Reynolds-Averaged Navier-Stokes (RANS) model used in the DDES method is the SST $k-\omega$ turbulence model [22-23]. The simulation process begins with unsteady numerical simulation of the flow field around the simplified train model. This step captures the flow field information near the model, which serves as the sound source term. Subsequently, the sound field information is derived using the FW-H equation, and The acoustic source integration surface is the solid surface. The FW-H equation can be mathematically expressed in the following form of Eq. (1):

$$\frac{1}{a_0^2}\frac{\partial^2 p'}{\partial t^2}-\nabla^2 p'=\frac{\partial^2}{\partial x_i \partial x_j}\{T_{ij}H(f)\}-\frac{\partial}{\partial x_i}\{[P_{ij}n_j+\rho u_i(u_n-v_n)]\delta(f)\} \tag{1}$$

$$+\frac{\partial}{\partial t}\{[\rho_0 v_n + \rho(u_n - v_n)]\delta(f)\}$$

where u_i is the component of the velocity of the fluid in the x_i direction, u_n represents the component of fluid velocity in the normal direction of the wall, v_i denotes the component of the surface velocity in the x_i direction, and v_n stands for the component of surface velocity along its normal direction. The terms $\delta(f)$ and $H(f)$ are the Dirac function, and the Heavyside's unit function, respectively.

The term p' is the far-field sound pressure. If $f = 0$, it represents a mathematical surface embedded in the unbounded space of the external flow problem ($f > 0$), so that it can be solved easily using generalized function theory and free space Green's function.

The term a_0 is the far-field sound speed, and T_{ij} is the Lighthill stress tensor, defined by Eq. (2):

$$T_{ij} = \rho u_i u_j + P_{ij} - a_0^2(\rho - \rho_0)\delta_{ij} \tag{2}$$

where P_{ij} is the compressive stress tensor. For Stokesian fluids, the compressive stress tensor is given by Eq. (3):

$$P_{ij} = p\delta_{ij} - \mu[\frac{\partial u_i}{\partial x_j} + \frac{\partial u_j}{\partial x_i} - \frac{2}{3}\frac{\partial u_k}{\partial x_k}\delta_{ij}] \tag{3}$$

The pressure-velocity coupling is solved using the Semi-Implicit Method for Pressure-Linked Equations (SIMPLE) algorithm. The discretized algebraic equations are solved through Gauss-Seidel iterations. During the unsteady flow field calculations, a physical time step of 1 × 10-4 seconds is adopted, with 20 internal iterations per time step to ensure the convergence criteria. The analyses cover a frequency range from 100 Hz to 5000 Hz.

To obtain numerical results, a computational domain is designed and sized with the train height H as the reference value, as shown in Figure 2. The inlet of the computational domain is positioned 15H away from the nose cone of the head car, while the outlet is 30H away from the nose cone of the tail car. Consequently, the total length of the computational domain in the X-direction is 66.5H. As centered on the central axis of the train cross-section, the width of the computational domain in the Y-direction is 32H. The height of the computational domain in the Z-direction is 20H above the rail's ground surface as the reference level.

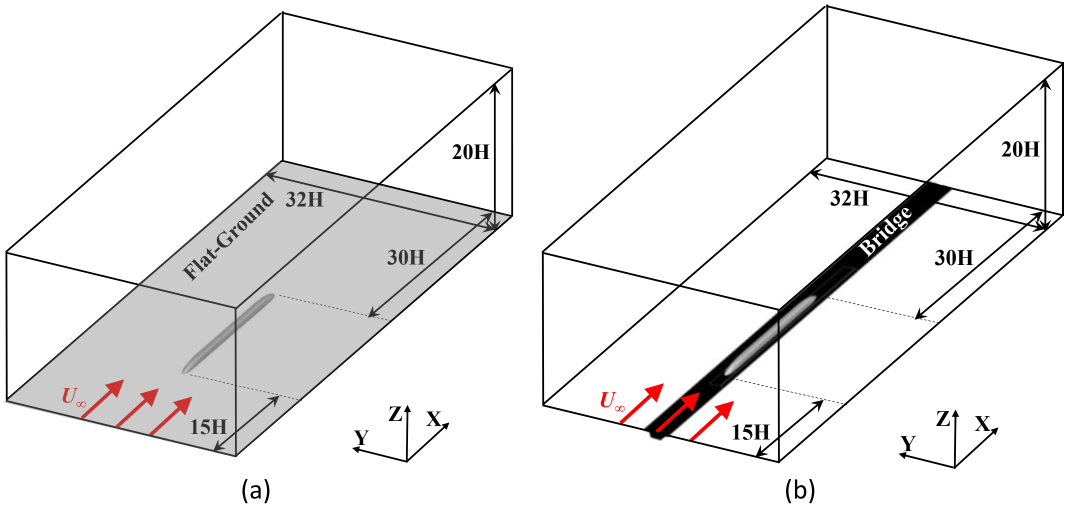

Figure 2 Schematic diagram of the computational domain ((a) Flat-ground modelling front view; (b) Bridge modelling front view).

The boundary conditions for the computational domain are set as follows: the velocity inlet for the inlet, and the pressure far field for the outlet and far fields. The air is treated as an ideal and compressible gas. The speed is given as negative train running speed, and U_∞ = 111.11 m/s is used in this paper. The Reynolds number based on the train height is 2.81×10^7. The boundary conditions for the train body surface are specified as no-slip and no-penetration solid wall. The ground plane, track surface on bridges, and other wall facilities (e.g., anti-collision walls) are all defined as slip walls, where the slip velocity is set to the incoming flow velocity.

Figure 3 and Figure 4 show the computational meshes adopted for the flat-ground modelling and the bridge modelling, respectively. Both employ a Cartesian mesh (predominantly hexahedral) with a three-layer refinement zone surrounding the train to capture the complex details of the flow field surrounding the train. The maximum mesh size is set at 4.0 mm for the streamlined parts of the train's head and tail cars, 8.0 mm for the smoothed parts of the head and tail cars, the windscreen, and the middle car, and 2.0 mm for the bogie areas. To further capture the boundary layer characteristics, a 10-layer boundary layer mesh is implemented on the train's surface, with the first layer height set at $10^{-4}H$ as H is the train height. The y+ values near the wall are all less than 1.

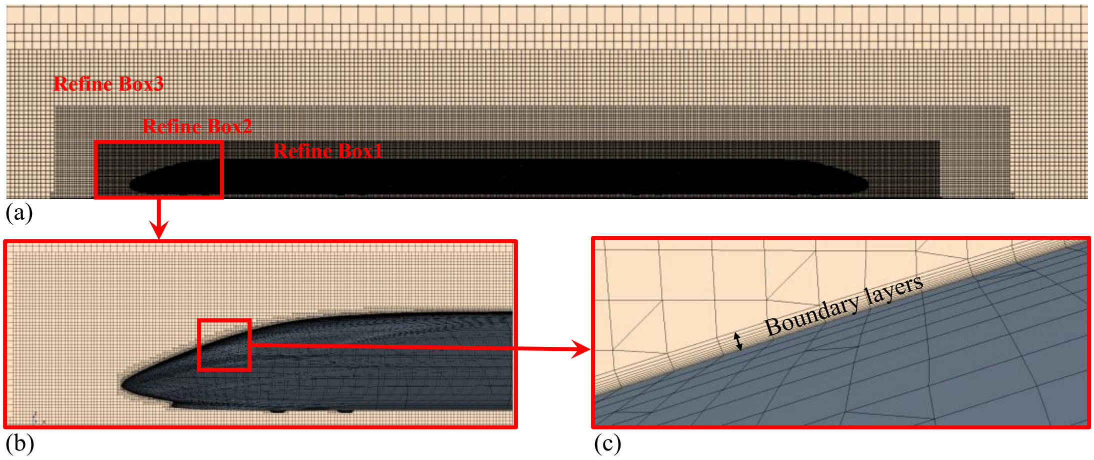

Figure 3 Details of computational mesh for the flat-ground modelling: (a) Lateral view of the entire train, (b) Lateral view of the head car, (c) Local enlarged view.

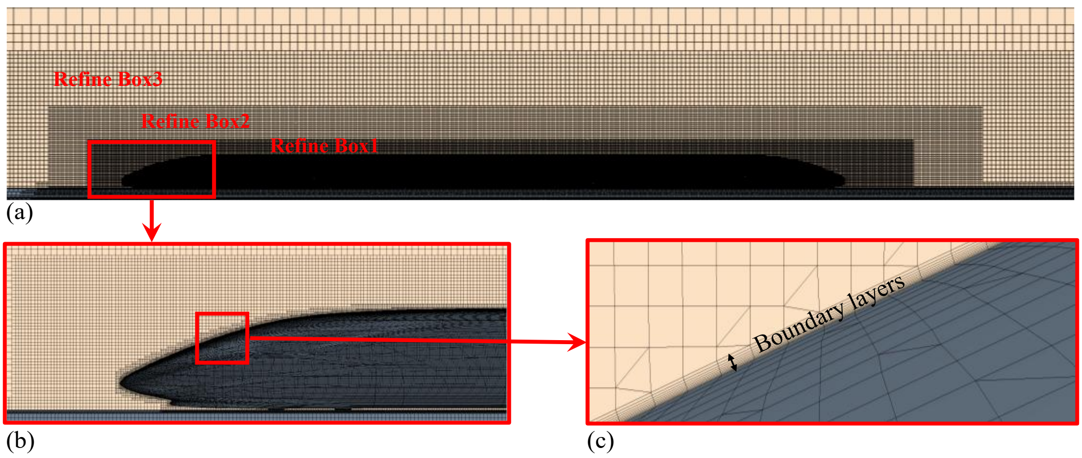

Figure 4 Details of computational mesh for the bridge modelling: (a) Lateral view of the entire train, (b) Lateral view of the head car, (c) Local enlarged view.

2.3. Simulation Verification

To verify the reliability of the numerical simulation method employed in this study, the tandem double-cylinder model, which was previously utilized in NASA's BART and QFF wind tunnel experiments [24], is adopted as the verification model for aerodynamic noise simulation. The diameter (D) of each cylinder is 0.05715 m and the spacing distance (L) between the two cylinders is set to 3.7D.

The mesh independence and numerical validation are done by three distinct grid numbers with different elements. Specifically, the coarse, medium, and dense grids contain 1.58 million cells, 3.52 million cells, and 7.32 million cells, respectively. Accordingly, the heights of the first layer of the grid in the near-wall region are 5×10-

4D, 1×10-4D, and 5×10-5D for the coarse, medium, and dense grids, respectively. The simulation methods applied in this verification are consistent with those described in Subsection 2.2 above.

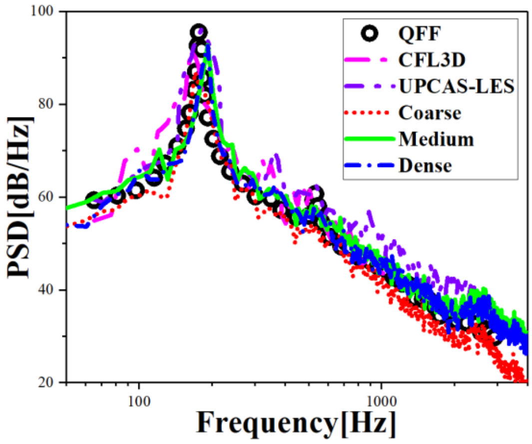

Figure 5 Verification results of double-cylinder noise calculation.

Figure 5 shows a comparison of the simulation results obtained from the three grid numbers using the previously described simulation methods and the experimental data from the reference [24]. Clearly, both the medium and dense grids can accurately capture the amplitude of broadband noise, as well as the characteristic frequency and amplitude of narrowband noise. The numerical results obtained from these two grid sets agree well with the experimental data and other computational results reported in the reference [24], with amplitude errors of less than 3%. This indicates that the medium and dense grids, along with the aerodynamic noise simulation methods employed in this study, are reliable and effective. Compared with the results obtained from the medium and dense grids, the coarse grid provides lower broadband noise results, especially in the high frequency range.

In addition, cavity noise verification was performed. The experiments were conducted in the D5 aeroacoustic wind tunnel at Beihang University [25] at a Mach number of 0.16. The temperature T_∞ and pressure P_∞ were 303 K s and 101325 Pa, respectively. Near-field noise was measured using a G.R.A.S. 1/4" surface microphone flush-mounted on the bottom wall of the cavity. The cavity dimensions are 200 mm in length, 600 mm in width, and 300 mm in depth. The cavity model was validated using three sets of meshes with different element counts. All three grids share the same topology. The total cell numbers are 2.1 million, 4.3 million, and 7.6 million, respectively. The first-layer mesh height is the same as that used for the cylindrical model.

Figure 6 shows the comparison results on the bottom surface, where several narrowband peaks are superimposed on the broadband spectrum. Compared with the experimental data [25], the coarse mesh exhibits significant errors at high frequencies.

When the mesh resolution is increased to the medium and fine levels, the simulated broadband noise intensity agrees well with the experimental results. Moreover, all numerical simulations successfully capture the frequencies corresponding to the narrowband tones, with errors in the dominant tone intensity below 3%.

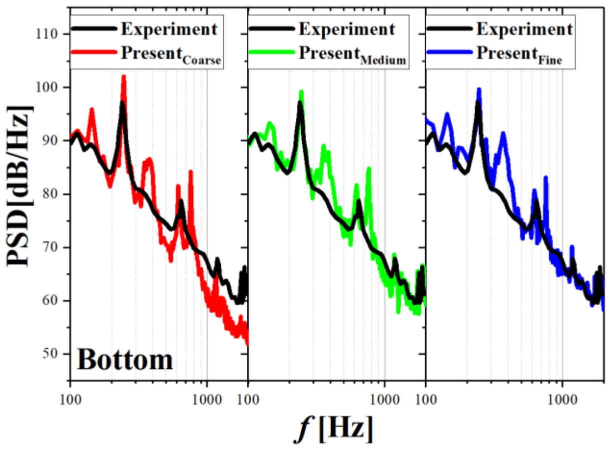

Figure 6 Comparison of power spectral density of the near-field sound pressure monitoring point placed at the bottom surface between experimental results and numerical simulation results calculated by three computational grids.

Therefore, based on the premise of the calculation accuracy and the limited computing resources, the grids in the subsequent simulations are generated according to the setting of the medium grid. The medium grid for a full-scale high-speed train has approximately 42 million elements, and the height of the first layer of the grid in the near-wall region is $10^{-4}H$.

3 Results

3.1 Analysis of near-filed sound source characteristics

In this subsection, we analyze the variation patterns of the train's near-field sound sources.

Figure 7 and Figure 8 show the surface sound power level distributions for flat-ground modeling and bridge modeling, respectively. The surface sound power (W) is calculated by Eq. (4):

$$W = \frac{p^2}{\rho c} \cdot 4\pi r^2 \tag{4}$$

where r is the height of the first layer grid, c is the sound speed, ρ is the air density, and p is the sound pressure. According to the definition of sound pressure, sound pressure is the fluctuation value of wall pressure. The surface pressure of the model can be obtained directly through CFD calculation. The instantaneous value of pressure minus the time-averaged value is its fluctuation value. Then, the sound power level is computed by Eq. (5):

$$Sound\ power\ level = 10\ log\ (\frac{W}{W_0}) \tag{5}$$

where W_0 is the reference acoustic power, 10-12 Watt.

Comparing Figure 7 (a) with Figure 8 (a) from the lateral view, the sound power level under flat-ground modeling is higher than that under bridge modeling, particularly beneath the streamlined section of the head car, as indicated by the pink box in these figures. From the top view in Figure 7 (b) with Figure 8 (b), the sound power level on the roof of the streamlined head region is higher under flat-ground modeling, also marked by the pink box; however, near the nose cone of the tail car, the sound power level under flat-ground modeling is lower than that under bridge modeling, as shown in the purple box. From the bottom view in Figure 7 (c) with Figure 8 (c), the sound power level across the train underbody is consistently higher under flat-ground modeling compared to bridge modeling.

It can be observed that, except for the region near the tail car nose cone, the sound power level under flat-ground modeling is generally higher than that under bridge modeling. This indicates that the sound source intensity is greater under flat-ground modeling than under bridge modeling.

Based on the near-field 1/3 octave A-weighted sound pressure level spectrum distribution (Figure 9), we investigate why the sound source intensity under flat-ground modeling is higher than under bridge modeling. The 1/3 octave A-weighted sound pressure level is calculated as follows:

$$L_A = 10lg\sum_{i=1}^{n} 10^{0.1}(L_{pi} + \Delta A_i) \tag{6}$$

Here, L_A represents the A-weighted sound level in dB(A), L_{pi} represents the sound pressure level in the i-th octave band in dB, and ΔA_i is the attenuation value of the i-th frequency A-weighting network.

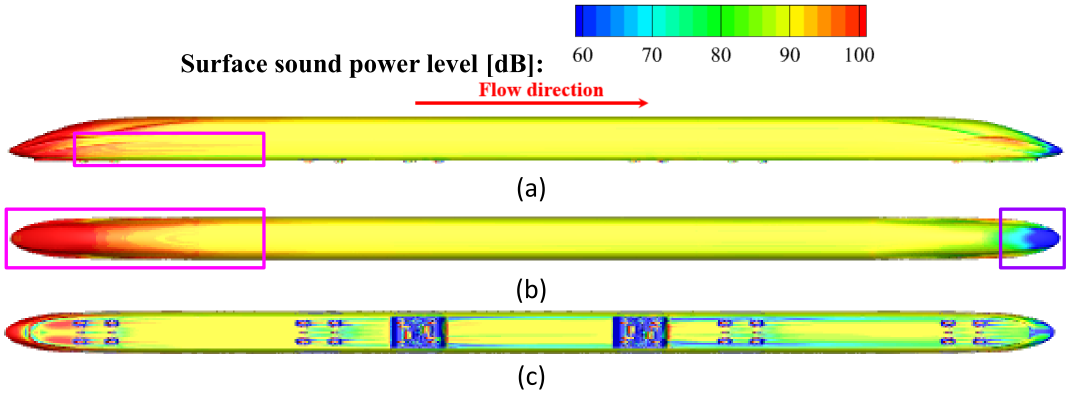

Figure 7 Surface sound power level of high-speed trains for flat-ground modelling ((a) Lateral view; (b) Top view; (c) Bottom view).

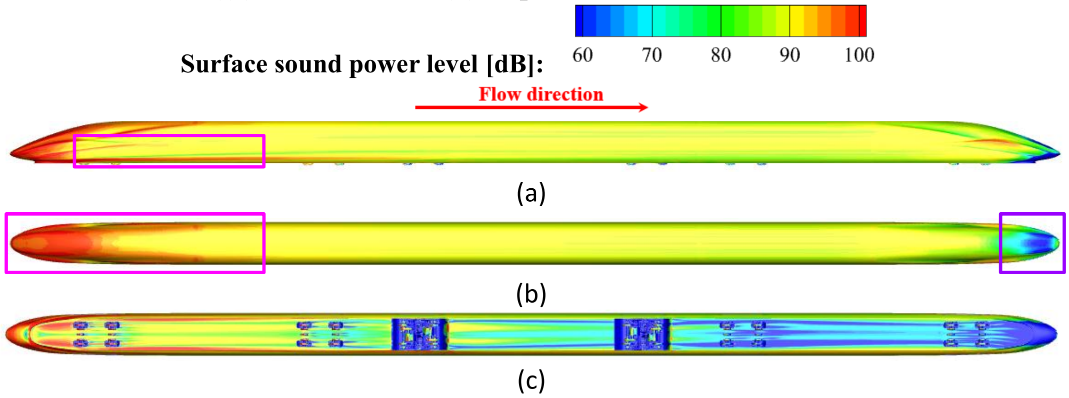

Figure 8 Surface sound power level of high-speed trains for bridge modelling((a) Lateral view; (b) Top view; (c) Bottom view).

From the 1/3 octave A-weighted sound pressure level spectrum at the nose cone of the head car (corresponding to S1 in Figure. **1**(a)) shown in Figure 9(a), the following observations can be made: Below 200 Hz and above 2000 Hz, the spectral intensity under bridge modeling is higher than that under flat-ground modeling, as indicated by the red shaded areas. In contrast, within the mid-frequency range of 250 Hz to 1600 Hz, flat-ground modeling exhibits higher spectral intensity, as shown by the gray shaded areas. Moreover, the spectral peaks for both modeling approaches occur within this frequency range. Consequently, from the perspective of overall sound pressure level, the sound source strength is stronger under flat-ground modeling. Additionally, Figure 9 (a) indicates that, compared with bridge modeling, the acoustic energy under flat-ground modeling is more concentrated in the mid-frequency range.

Figure 9 (b) shows the 1/3 octave A-weighted sound pressure level spectrum at the midpoint of the middle car (corresponding to S2 in Figure. **1** (a)). The result is similar to that in Figure 9 (a), with two notable differences: first, in the high-frequency range (above 2000 Hz), the spectral amplitude at this location is higher under flat-ground modeling than under bridge modeling; second, in the low-frequency range, the spectral amplitude at the midpoint of the middle car is significantly stronger than that at the nose cone of the head car for both modeling approaches.

Figure 9 (c) shows the 1/3 octave A-weighted sound pressure level spectrum at the nose cone of the tail car (corresponding to S3 in Figure. **1** (a)). Its trend is largely consistent with that in Figure 9 (a), but the spectral amplitudes across all frequency bands are relatively lower.

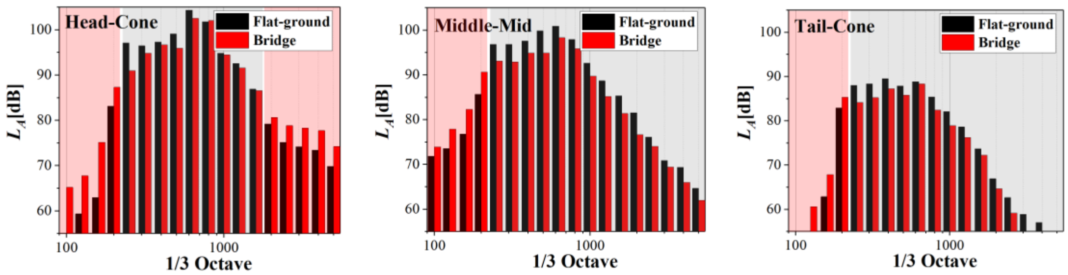

(a) (b) (c)

Figure 9 A-weighted sound pressure levels at different positions on the near-field vehicle surface ((a) Front car nose cone; (b) Mid-point of middle car; (c) Tail car nose cone).

In summary, based on Figure 9:

- The peak spectral amplitude is highest at the nose cone of the head car, indicating that the sound source intensity is strongest at this location among different locations along the train body.
- Compared with bridge modeling, flat-ground modeling concentrates acoustic energy more in the mid- and high-frequency ranges. Since the spectral peaks occur in the mid-frequency range, flat-ground modeling results in stronger overall sound source intensity.
- Bridge modeling leads to an increase in high-frequency acoustic energy near the nose cone of the head car.

Figure 10 presents the surface sound power values of various components/areas of the train, providing further insight into the influence of ground modeling approaches on the acoustic source characteristics. Regardless of the ground modeling approach, the strongest sound source intensity is observed in the lower part of the head car, followed by the upper part of the head car, and the entire head-car region generally exhibits high acoustic source levels. This observation aligns with the results shown in Figures 7 to 9. Moreover, the sound source intensity under flat-ground modeling is essentially higher than that under bridge modeling. This indicates that not only at the three positions analyzed in Figure 9, but across all components/areas of the entire train, acoustic energy is more concentrated in the mid-frequency range under flat-ground modeling—i.e., the frequency band where spectral peaks occur.

Figure 11 shows the surface sound power percentage of different components/areas of the train. It can be seen that, although the absolute value of sound source intensity under flat-ground modeling is higher than that under bridge modeling for all components/areas of the entire train, the relative variation in "sound power percentage" follows a different pattern. First, for all height zones (head car, middle car, and tail car), the sound power percentage under bridge modeling is higher than that under flat-ground modeling. This indicates that, although the overall sound source intensity is lower under bridge modeling, the contribution and proportion from the car body increase.

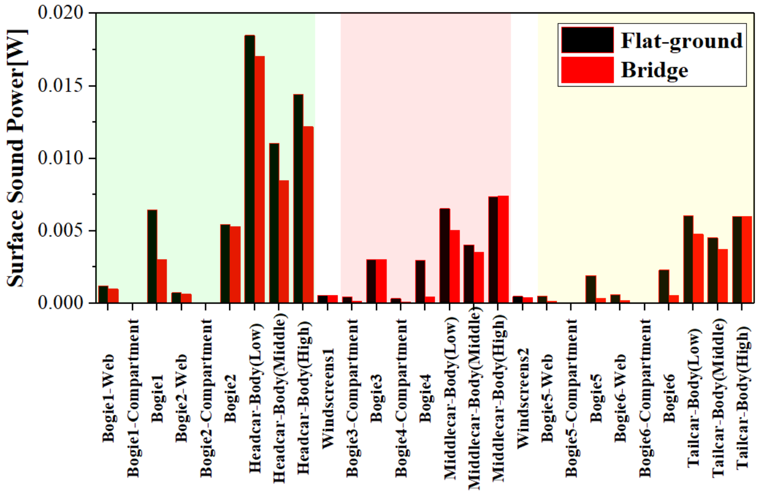

Figure 10 Surface sound power of different components/areas.

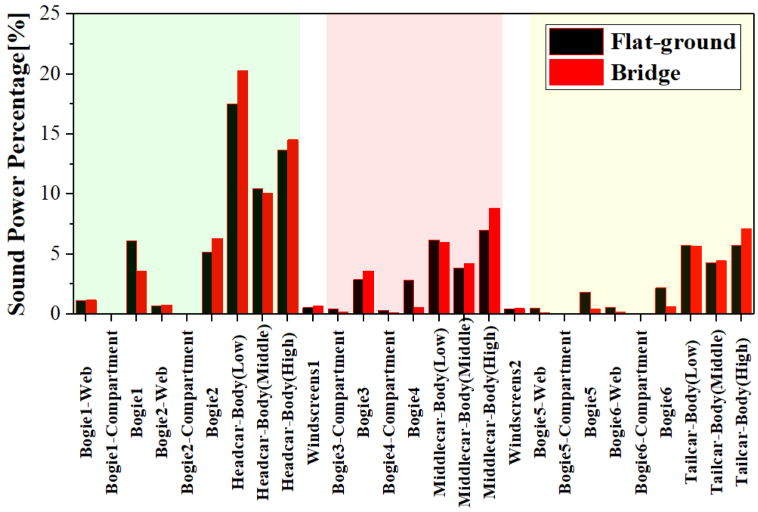

Figure 11 Surface sound power percentage of different components/areas.

3.2 Analysis of far-filed noise characteristics

The previous subsection analyzed the influence of ground modeling approaches on near-field sound sources. This subsection examines the impact of ground modeling approaches on far-field noise.

Figure 12 presents the overall sound pressure level of the far-field noise at a height of 3.5 m and a lateral distance of 25 m from the train's central axis. A total of 11 points were arranged along the flow direction at intervals of 10 m.

The variation trend of the far-field overall sound pressure level along the flow direction shows that, at all 11 points, the overall sound pressure level of the high-speed train under flat-ground modeling is consistently higher than that under bridge modeling. Additionally, both overall sound pressure level curves gradually decrease in the downstream direction. The difference between the two curves is minimal at X = -50 m, amounting to less than 1 dB. As the measurement extended downstream, the difference gradually increases, reaching a maximum of approximately 4 dB at X = 50 m.

Figure 13 presents the 1/3 octave A-weighted sound pressure level spectra of the entire high-speed train at three far-field locations: X = –40 m, 0 m, and 40 m. Similar to the near-field spectral distributions shown in Figure 9, Figure 13 (a) and Figure 13 (b) indicate that below 200 Hz and above 2000 Hz, the spectral intensity under bridge modeling is higher than that under flat-ground modeling (as represented by the red shaded areas). Conversely, within the mid-frequency range of 250 Hz to 1600 Hz, the spectral intensity under flat-ground modeling is greater (as indicated by the gray shaded areas), and the spectral peaks for both modeling approaches also appear in this frequency range. Consequently, from the perspective of overall sound pressure level, the far-field noise intensity is stronger under flat-ground modeling, and its acoustic energy is relatively more concentrated in the mid-frequency range. Figure 13 (c) further demonstrates that in the high-frequency range, the spectral intensity under flat-ground modeling is also higher than that under bridge modeling, and the difference between the two increases with frequency. This difference in high-frequency acoustic energy, combined with the aforementioned mid-frequency peak disparity, jointly explains the gradual increase in the difference between the two overall sound pressure level curves along the downstream direction observed in Figure 12.

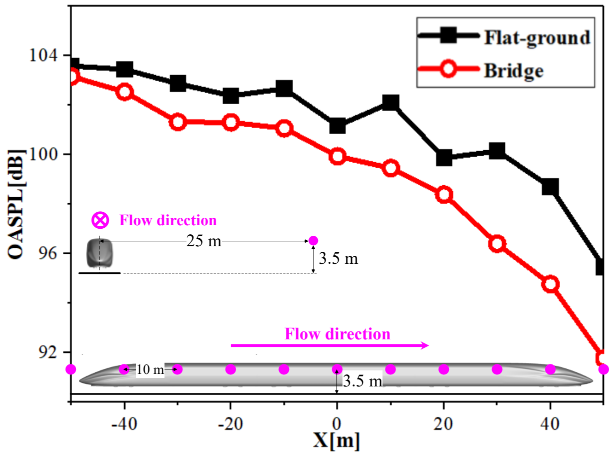

Figure 12 Overall sound pressure level at different standard measurement points in the far field.

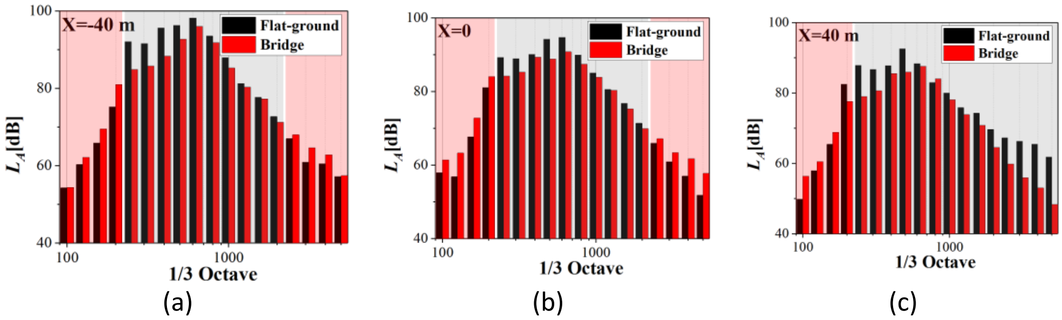

Figure 13 A-weighted sound pressure levels at different standard measurement points in the far field ((a) X = -40 m; (b) X = 0 m; (c) X = 40 m).

Figure 14 (a) shows the variation of the far-field noise equivalent continuous A-weighted sound pressure level ($L_{A,eq}$) with frequency. The $L_{A,eq}$ is calculated according to the international standard ISO 3095:2025 using the following formula [26]:

$$L_{A,eq} = 10\lg\left(\frac{1}{t_2 - t_1}\int_{t_1}^{t_2}\frac{p_A^2(t)}{p_0^2}\,\mathrm{d}t\right) \tag{7}$$

Here, t_1 and t_2 represent the start and end times of the train passage, respectively. The start and end times are defined as the moments when the short-term pass-by noise is 10 dB(A) below the average A-weighted sound level of the train passage. In this study, a space-for-time substitution method is adopted. p_A denotes the measured sound pressure, and p_0 is the reference sound pressure (2×10-5 Pa).

The distribution of $L_{A,eq}$ across frequency bands in Figure 14 (a) largely follows the trend observed in Figure 13 (a): under flat-ground modeling, acoustic energy is primarily concentrated in the mid-frequency range, while under bridge modeling, it is dispersed across both low and high-frequency bands.

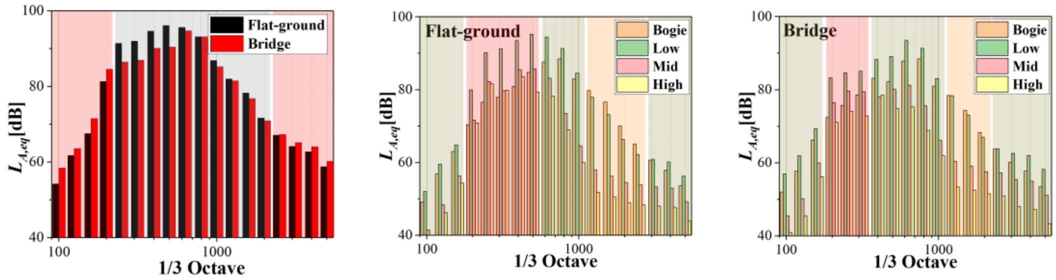

(a) (b) (c)

Figure 14 Far-field equivalent continuous A-weighted sound pressure level ((a) Total noise from high-speed train; (b) High-speed train bogie area and different height zones for flat-ground modelling; (c) High-speed train bogie area and different height zones for bridge modelling).

Figure 14 (b) and Figure 14 (c) present the variation of the far-field $L_{A,eq}$ with frequency for the two modeling approaches. The bogie area (including webs, six bogies, and the bogie cavity), the lower zone, the middle zone, and the higher zone are treated as integrated sound sources to analyze the contribution of different regions to far-field noise. The contribution distribution is as follows:

- In the low-frequency range, the lower zone contributes the most under both modeling approaches, followed by the bogie area.
- In the low-mid frequency range, the lower zone remains the dominant contributor, with the middle zone ranking second.
- In the mid-frequency range, the lower zone again contributes the most, followed by the bogie area.
- In the mid-high frequency range, the bogie area becomes the primary contributor, followed by the lower zone.
- In the high-frequency range, the lower zone contributes the most, with the bogie area again ranking second.

Summarising Figure 14 reveals:

- In the low- and high-frequency bands, the far-field $L_{A,eq}$ under bridge modeling is higher than that under flat-ground modeling, with the main contributions coming from the lower zone and the bogie area. In the mid-frequency band, however, the far-field $L_{A,eq}$ under flat-ground modeling is higher, mainly due to contributions from the lower zone, middle zone, and bogie area. This indicates that the variation of far-field $L_{A,eq}$ with frequency does not stem from a simple shift of a single local sound source, but rather reflects the overall spectral characteristics of the broadband noise from different regions under the influence of the modeling approach.
- Since the lower zone exhibits the highest sound source intensity, its impact on far-field noise is the most significant. Bridge modeling reduces the spacing between the train underbody and the track surface, lowering the flow velocity and turbulent kinetic energy, thereby decreasing the overall

underbody noise intensity. At the same time, the vortex structures beneath the train become more fragmented, while the size of the overflow vortices on both sides of the train increases, leading to enhanced noise intensity in the lower zone within the low- and high-frequency bands. These acoustic changes in the lower zone directly dominate the alteration of the overall train noise characteristics.

4 Conclusions and Contributions

Based on a comprehensive analysis of the sound field, the following conclusions can be drawn, revealing the mechanism by which different ground modeling methods affect the aerodynamic noise of high-speed trains:

(1) The underbody region is the key contributor to overall noise in both modeling approaches. Flat-ground modeling results in generally higher near-field sound source intensity than bridge modeling, as acoustic energy is more concentrated in the mid-frequency range (250–1600 Hz) where spectral peaks occur. This trend holds across most train components, including the streamlined head, roof, and underbody, except near the tail car nose cone. Although absolute sound power values are higher under flat-ground modeling, the car body's relative contribution is greater under bridge modeling.

(2) Spatial variation of far-field noise arises from the coupling effect of spectral structure and regional contributions. Far-field noise exhibits lower overall sound pressure levels under bridge modeling, but the gap compared to flat-ground modeling gradually widens downstream, reaching a maximum of approximately 4 dB. This trend is jointly caused by differences in mid-frequency acoustic energy peaks and contributions from high-frequency acoustic energy.

Acknowledgements

This work was supported by National Key Research and Development Program (Grant No. 2022YFB2603400).

References

[1] LI Z., WANG Q., CAI M., et al. Impacts of high-speed rail on the industrial developments of non-central cities in China[J]. Transport Policy, 2023, 134, 203-216.
[2] XIONG J., SHEN Z.. Rise and future development of Chinese high-speed railway[J]. Journal of Traffic and Transportation Engineering, 2021, 21(5): 6-29.
[3] LEMAITRE G., AUBIN F., LAMBOURG C., et al. Annoyance of interior noise in high-speed trains: Determining acceptability thresholds for different passenger activities[J]. J. Acoust. Soc. Am., 2025, 158, 1189–1203.

[4] LUO W., WANG H., LI Z., et al. Influence of enlarged cross-section railway tunnels on the aerodynamic noise source characteristics of high-speed trains[J]. Physics of Fluids, 2025, 37, 065144.
[5] YU H., LI J.. ZHANG H. On aerodynamic noises radiated by the pantograph system of high-speed trains[J]. Acta Mech Sin, 2013, 29, 399–410.
[6] TALOTTE, C.. Aerodynamic noise: a critical survey[J]. Journal of Sound and Vibration, 2000, 231(3), 549-562.
[7] ZHANG J, DING Y, WANG Y, et al. A novel bionic Coleoptera pantograph deflector for aerodynamic drag reduction of a high-speed train[J]. Journal of Central South University, 2023, 30(6): 2064-2080.
[8] ZHAO Y., YANG Z., LI Q., et al. Analysis of the near-field and far-field sound pressure generated by high-speed trains pantograph system[J]. Applied Acoustics, 2020, 169:107506.
[9] HE, Y., THOMPSON, D., HU, Z.. Aerodynamic noise from a high-speed train bogie with complex geometry under a leading car[J]. Journal of Wind Engineering and Industrial Aerodynamics, 2024, 244, 105617.
[10] SHI L., ZHANG C., WANG J., et al.Numerical Analysis of Aerodynamic Noise of a High-Speed Pantograph[A]. 2013 Fourth International Conference on Digital Manufacturing and Automation[C]. Shinan, China, 2013.
[11] PLENTOVICH E. B., STALLINGS R. L., TRACY M.B.. Experimental cavity pressure measurements at subsonic and transonic speeds, Static-pressure results[R]. 1993, Technical Paper No. TP-3358 (NASA Langley Research Center, Hampton, VA).
[12] TAN X., XIE P. YANG Z., et al. Adaptability of Turbulence models for pantograph aerodynamic noise simulation[J]. Shock and Vibration, 2019, 2019:1-20.
[13] LI Q, LI Z, YANG Z. Noise contribution and coherence analysis of high-speed train head shape under moving slab track[J]. Proceedings of IMechE Part F: Journal of Rail and Rapid Transit, 2023, 237(7): 848-857.
[14] TAN X., LIU H., YANG Z., et al. Characteristics and mechanism analysis of aerodynamic noise sources for high-speed train in tunnel[J]. Complexity, 2018, 2018:1-19.
[15] LATORREIGLESIAS E., THOMPSON D., MUÑOZ PANIAGUA J., et al. On the feasibility of a component-based approach to predict aerodynamic noise from high-speed train bogies[J]. Applied Acoustics, 2023, 211, 109536.
[16] ZHU J., HU Z.. Flow between the train underbody and trackbed around the bogie area and its impact on ballast flight[J]. Journal of Wind Engineering and Industrial Aerodynamics, 2017, 166, 20–28.
[17] ZHANG D., LI H., ZHOU, F., et al. A convolutional neural network driven suspension control strategy to enhance sustainability of high-speed trains[J]. Energy Conversion and Management: X, 2025, 27, 101183.
[18] LI Z., LI Q., YANG Z.. Research on jet control and noise reduction mechanism of sound source for leading bogie region[J]. Applied Acoustics, 2025, 232, 110567.
[19] DENG, E., YANG, W., DENG, L., et al. Time-resolved aerodynamic loads on high-speed trains during running on a tunnel-bridge-tunnel infrastructure under

crosswind[J]. Engineering Applications of Computational Fluid Mechanics, 2019, 14(1), 202–221.
[20] PAZ C., SUÁREZ E., GIL C. Numerical methodology for evaluating the effect of sleepers in the underbody flow of a high-speed train. Journal of Wind Engineering and Industrial Aerodynamics, 2017, 167, 140–147.
[21] THOMPSON D.. Railway Noise and Vibration: Mechanisms, Modelling and Means of Control[M]. 2nd ed. London: ELSERIER, 2024.
[22] WANG D., DU Y., JIN Y., et al. Comparative study on predicting turbulent kinetic energy budget using high-order upwind scheme and non-dissipative central scheme[J]. Adv. Aerodyn., 2024, 6, 24.
[23] ZHAO L., DENG E., YANG W., et al. Unraveling the impact of cutting transition section on the aerodynamic loads of high-speed trains: Utilizing the IDDES approach[J]. Journal of Central South University, 2024, 31, 989-1002.
[24] NEUHART D., JENKINS L., CHOUDHARI M., et al. Measurements of the flowfield interaction between tandem cylinders[A]. 15th AIAA/CEAS Aeroacoustics Conference (30th AIAA Aeroacoustics Conference)[C]. Miami, Florida, 2009, AIAA-2009-3275.
[25] GUO Z., LIU P., GUO H.. Control effect on deep cavity noise by slanted walls at low Mach numbers[J]. Journal of Vibration and Control, 2021, 27(9-10):998-1008.
[26] ISO 3095:2025-Railway applications — Acoustics — Measurement of noise emitted by railbound vehicles.